Role of human Hv1 channels in sperm capacitation and white blood cell respiratory burst established by a designed peptide inhibitor

Ruiming Zhao[a,b,c,1], Kelleigh Kennedy[a,1], Gerardo A. De Blas[d], Gerardo Orta[e], Martín A. Pavarotti[d], Rodolfo J. Arias[d], José Luis de la Vega-Beltrán[e], Qufei Li[f], Hui Dai[a,b,c], Eduardo Perozo[f], Luis S. Mayorga[d], Alberto Darszon[e], and Steve A. N. Goldstein[a,b,c,2]

[a]Department of Biochemistry, Brandeis University, Waltham, MA 02453; [b]Department of Pediatrics, Loyola University Chicago Stritch School of Medicine, Maywood, IL 60153; [c]Department of Cell and Molecular Physiology, Loyola University Chicago Stritch School of Medicine, Maywood, IL 60153; [d]Instituto de Histología y Embriología de Mendoza (Consejo Nacional de Investigaciones Científicas y Técnicas–Universidad Nacional de Cuyo), School of Medicine, National University of Cuyo, Mendoza CP 5500, Argentina; [e]Departamento de Genética del Desarrollo y Fisiología Molecular, Instituto de Biotecnología, Universidad Nacional Autónoma de México, 62250 Morelos, México; and [f]Department of Biochemistry and Molecular Biology, Gordon Center for Integrative Science, University of Chicago, Chicago, IL 60637

Edited by Richard W. Aldrich, The University of Texas at Austin, Austin, TX, and approved October 29, 2018 (received for review September 18, 2018)

Using a de novo peptide inhibitor, Corza6 (C6), we demonstrate that the human voltage-gated proton channel (hHv1) is the main pathway for H^+ efflux that allows capacitation in sperm and permits sustained reactive oxygen species (ROS) production in white blood cells (WBCs). C6 was identified by a phage-display strategy whereby ∼1 million novel peptides were fabricated on an inhibitor cysteine knot (ICK) scaffold and sorting on purified hHv1 protein. Two C6 peptides bind to each dimeric channel, one on the S3–S4 loop of each voltage sensor domain (VSD). Binding is cooperative with an equilibrium affinity (K_d) of ∼1 nM at −50 mV. As expected for a VSD-directed toxin, C6 inhibits by shifting hHv1 activation to more positive voltages, slowing opening and speeding closure, effects that diminish with membrane depolarization.

proton channel | C6 | ICK | venom | TIRF

The human voltage-gated proton channel (hHv1) is thought to play critical roles as a H^+ proton efflux pathway in both normal biology and the pathogenesis of common disorders based on its biophysical characterization and the effects of its knockout in transgenic mice (1–3). hHv1 channels are formed by two identical subunits each with four transmembrane spans (TMs) that resemble the voltage sensor domains (VSDs) in other voltage-gated ion channels (VGICs) and lack the two additional TMs that contribute to forming the ion conduction pores in those channels (4, 5). Unlike other VGICs, hHv1 has a H^+-selective conduction pathway within the VSD of each subunit (6, 7). Studying the operation of the channel has been impeded since known inhibitors are indiscriminate and weak suppressors (8–10).

Inhibitor cysteine knot (ICK) peptides in the venoms of spiders, scorpions, and snails are rich in VSD-directed toxins that modify channel gating (that is, opening and closing) (11–13). Recognized by a protein fold stabilized by three disulfide bonds, most ICK toxins inhibit by binding to extracellular sites on VGICs "trapping" the VSDs so they are unable to move normally in response to changes in transmembrane voltage (14, 15).

In the past, we designed phage-display libraries based on toxin peptide scaffolds that target the ion conduction pores in potassium channels to identify a high-affinity blocker with greater specificity for the Kv1.3 voltage-gated channel (16) and for KcsA, a channel that had no known regulator (17). Here, we describe the development and use of Corza6 (C6), a high-affinity, specific inhibitor of hHv1, to demonstrate the roles of hHv1 in native human sperm and white blood cells (WBCs) proposed by others (18–21). Seeking to harness VSD-directed inhibitory mechanism to regulate hHv1, we constructed a phage-display library of 1,047,280 variants based on the ICK scaffold and sorted on purified hHv1 protein. C6 was identified and characterized as a potent and specific inhibitor of hHv1 using electrophysiology and single-molecule total internal reflection fluorescent microscopy (smTIRF). C6 binds to the loop between the third and fourth membrane spans in the channel (S3–S4 loop), a segment that confers inhibition to a C6-insensitive proton channel [*Ciona intestinalis* Hv1 (CiHv1)] when transplanted from hHv1.

C6 was used to evaluate two examples where the lack of a selective hHv1 inhibitor had impeded confirmation of the role of Hv1 in humans. Lishko et al. (18, 22) argue convincingly that hHv1 is required for capacitation and the subsequent acrosomal reaction in human sperm cells but comment on the need for a specific inhibitor to validate their hypotheses because available reagents were nonspecific and mouse sperm do not require mHv1 for fertility (18, 20, 23). Several groups (20, 21, 23, 24) have proposed that Hv1 is required to achieve sustained reactive oxygen species (ROS) production in human phagocytic WBCs based on the substantial reduction of the response in $mHv1^{-/-}$ mice during respiratory burst, while recognizing that compensatory changes in transgenic animals leave open alternative mechanisms in mice and the possibility for different pathways in humans, as observed in

Significance

Some peptide toxins act by stabilizing the voltage sensor domains (VSDs) of voltage-gated channels in open or closed conformations. hHv1 is a human voltage-gated proton channel and has lacked a specific inhibitor to assess its roles in physiology. We designed a phage-display library of 1 million novel peptides sharing an inhibitor cysteine knot (ICK) scaffold by combining elements of natural toxins; phagemids expressing Corza6 (C6) were selected by their capacity to bind to hHv1 protein. Two C6 peptides bind to the two VSDs in hHv1 and thereby inhibit channel operation. C6 was employed to confirm hypothesized roles for hHv1 in human sperm and white blood cells. The method should prove amenable to designer toxin identification for other voltage-gated channels.

Author contributions: R.Z., K.K., E.P., L.S.M., A.D., and S.A.N.G. designed research; R.Z., K.K., G.A.D.B., G.O., M.A.P., R.J.A., J.L.d.l.V.-B., Q.L., H.D., and S.A.N.G. performed research; and R.Z., K.K., E.P., L.S.M., A.D., and S.A.N.G. wrote the paper.

Conflict of interest statement: Based in part on this work, a patent application ("HV1 Modulators and Uses," PCT/US2017/068896) has been filed.

This article is a PNAS Direct Submission.

[1]R.Z. and K.K. contributed equally to this work.

[2]To whom correspondence should be addressed. Email: sgoldstein3@luc.edu.

This article contains supporting information online at www.pnas.org/lookup/suppl/doi:10.1073/pnas.1816189115/-/DCSupplemental.

Published online November 26, 2018.

sperm. Here, we settle the role of hHv1 in both human sperm capacitation, and phorbol myristate acetate (PMA)-activated ROS production in human WBCs, by studying the action of C6 on the channels in these native environments.

Results

An ICK Scaffold Library with over 1 Million Variants. The spider toxin ProTx-II (25) was chosen as the template for the design of the phage library based on its potent ability to impede the movement of voltage sensors in many VGICs. ProTx-II has 30 residues including six cysteines that form three disulfide bonds (CysI to CysIV, CysII to CysV, and CysIII to CysVI) to create and stabilize the ICK backbone (Fig. 1*A*) (26). To preserve the ICK architecture in designed toxins, the genes for 110 known and predicted toxins that appeared to employ the same arrangement of disulfide bonds were chosen from the sequences identified in a BLAST search using the protein sequence of ProTx-II as bait (*SI Appendix*, Table S1). The 110 protein sequences were aligned based on the six structural cysteines, and CysII and CysV were selected as the boundaries to define three domains, A, B, and C (Fig. 1*A*). Oligonucleotides were designed to encode for each of the unique domains in the 110 sequences yielding 95 A, 104 B, and 106 C domains. Unidirectional ligation allowed restricted permutations and recombination only in the correct order (A–B–C); this maintained the relative positions of the cysteines in the primary sequences and created a calculated diversity of 1,047,170 novel peptides as well as reproducing the 110 template sequences. The nucleotides for the peptides were ligated in-frame with phage coat protein pIII to expose the encoded peptides on the phage surface, as before in the pore-directed toxin scaffold libraries (16, 17).

Library Sorting on Purified hHv1 Isolates C6. A variant of hHv1 lacking portions of the N and C termini (hHv1-VSD) was purified and biotinylated as described before (27). The biotinylated hHv1 protein was immobilized on streptavidin-coupled magnetic beads or adhered directly in plastic wells in sequential panning rounds as the target for phage sorting as described in *Materials and Methods*. During each panning round, phages were incubated with immobilized hHv1 protein, poorly associated phages were separated from those more stably bound by washing, and then the bound phages were eluted and amplified for the next sorting step. After five rounds, phage enrichment was observed with hHv1 protein compared with control wells (Fig. 1*A*) and DNA sequencing of 48 clones identified the novel peptide C6 (Fig. 1*B*) that had been enriched out of the ∼1 million predicted variants. Of the enriched phagemids, 6.25% expressed C6, indicating an increase of ∼65,000-fold from its starting abundance. Supporting specific binding, phages expressing C6 were shown by ELISA to bind to immobilized hHv1 proteins in a stable and specific manner, whereas recovery was negligible in wells without target protein or with a control protein, streptavidin (Fig. 1*C*).

The A domain in C6 is from Omega-AcTx-Hv1b (28), a venom toxin from the funnel-web spider *Hadronyche versuta* that is lethal to crickets after lateroventral thoracic injection (Fig. 1*B*). The B domain in C6 is from JzTX21 (29), a peptide that is from the tarantula *Chilobrachys guangxiensis* and that is without a reported target or function. The C domain in C6 is from Hm2 (30), a venom toxin from crab spider *Heriaeus melloteei* that can inhibit the voltage-gated sodium channel Nav1.4 with an IC_{50} of ∼150 nM. The predicted C6 peptide was synthesized for study.

Two C6 Bind to Dimeric hHv1 Channels with Positive Cooperativity. C6 was isolated by binding to the purified hHv1 protein, which has been shown to be monomeric at the nanomolar concentrations employed in our panning condition (*Materials and Methods*) (27), rather than the full-length channel expressed in the native milieu of a cellular plasma membrane. We therefore sought evidence for C6 binding to intact hHv1 channels expressed in live HEK293T cells using smTIRF. The N terminus of C6 was labeled with the red fluorophore carboxytetramethylrhodamine (TAMRA-C6) and the C terminus of hHv1 was tagged with teal fluorescent protein (hHv1-TFP, Fig. 2*A*). Incubation of TAMRA-C6 with cells expressing hHv1-TFP produced particles containing both fluorescent colors at the cell surface (Fig. 2*B*). Cells subjected to illumination to achieve fluorophore bleaching allowed counting of the number of Hv1-TFP subunits and molecules of TAMRA-C6 present in each particle by methods we have described previously (31–33).

Two stepwise decreases in fluorescence were seen in 88% of particles with hHv1-TFP (Fig. 2 *B* and *C* and *SI Appendix*, Table S2), supporting other evidence that the majority of hHv1 channels are dimeric (34, 35). Consistent with fluorophore prebleaching and missed events at the time resolution of smTIRF system (31), we observed ∼10% of particles with single hHv1-TFP bleaching events. To validate our estimate of two subunits in hHv1 channels, we applied the statistical approach of Hines for inferring stoichiometry from photobleaching studies (36) to assess the probability of observing each fluorescence event (θ) and determined the confidence (estimated likelihood) that our conclusion was accurate to be >0.999 (*SI Appendix*, Table S2).

To measure the binding affinity of TAMRA-C6 toxin for hHv1-TFP channels, we varied the concentration of TAMRA-C6 applied to hHv1-TFP channels expressed in HEK293T cells. smTIRF was used first to study single fluorescent particles with both fluorophores to determine the fractional occupancy of channels by C6 on a pixel-by-pixel basis. When only 0.01 nM TAMRA-C6 was applied, surface particles of hHv1-TFP with

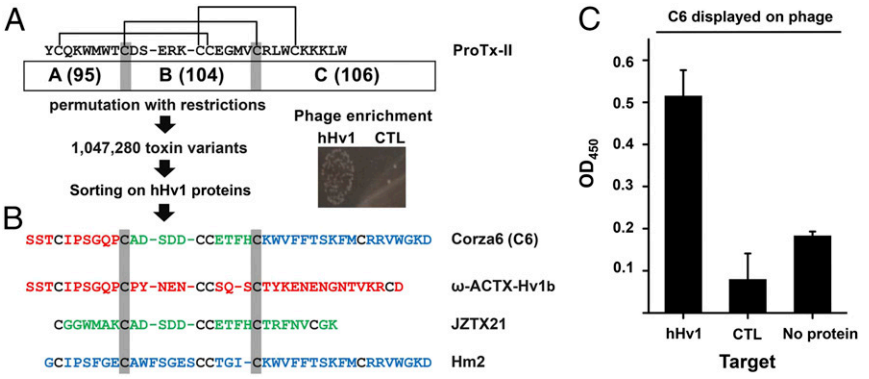

Fig. 1. C6 is isolated from an ICK scaffold, phage-display library. ICK scaffold phage library construction, hHv1 protein purification, phage preparation, and sorting are described in *Materials and Methods*. (*A*) Library design and phage sorting. A total of 110 ICK toxin sequences was aligned on conserved Cys residues (indicated by the gray highlighting) to define three domains that correspond to ProTx-II residues Tyr1–Thr8, Asp10–Val20, and Arg22–Trp30, respectively. Black lines indicate the arrangement of disulfide bridges. This yields 95, 104, and 106 unique A, B, and C domains, respectively (*SI Appendix*, Table S1), that combine to produce a calculated library diversity of ∼1 million for all natural and novel ABC peptides. After five rounds of selection on hHv1 protein, phage enrichment was observed compared with the streptavidin control. (*B*) Corza6 (C6) is a novel toxin isolated from the library screening. DNA sequencing revealed that C6 toxin phage had been enriched after phage sorting. C6 composed of residues present in three natural parental spider toxins, ω-ACTX-Hv1b (red), JZTX21 (green), and Hm2 (blue). (*C*) ELISA shows C6 phage binds to hHv1 protein but not control protein streptavidin and ELISA plate (no protein). The 96-well plates coated with or without target protein were incubated with C6 phage (10^{10}/well). Data are mean ± SD for three wells.

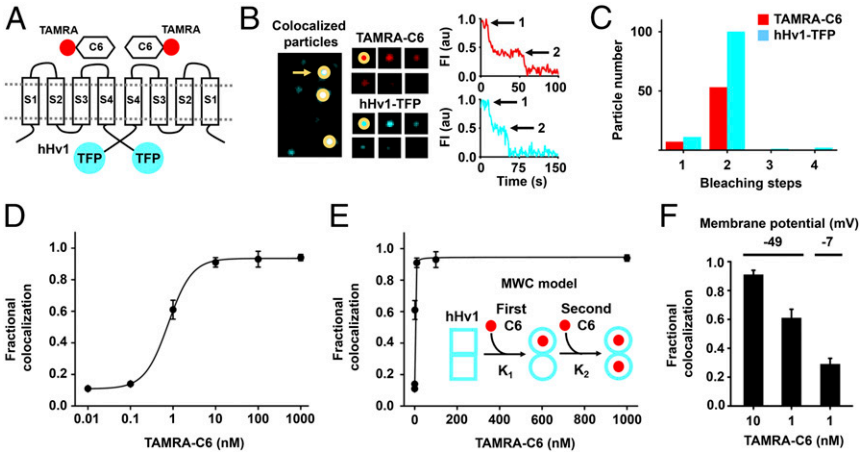

Fig. 2. C6 binds to cell surface hHv1 channels potently and cooperatively. C6 peptide was synthesized and labeled with red fluorophore carboxytetramethylrhodamine (TAMRA-C6) and studied with hHv1 tagged with teal fluorescent protein (hHv1-TFP) in HEK293T cells by smTIRF microscopy as described in *Materials and Methods*. (*A*) Cartoon showing two TAMRA-C6 peptides binding on two subunits of an hHv1-TFP–tagged channel. (*B*, *Left*) Incubation of TAMRA-C6 (red) with heterologous expressed hHv1-TFP (teal) results in single colocalized particles (white) with both TAMRA and TFP fluorescence at the surface of cells. (*B*, *Center*) Montage of photobleaching time course of a single fluorescent particle (indicated by arrow in *Left*), during continuous excitation to bleach the fluorophores. Every fifth frame is shown. (*B*, *Right*) Time courses for simultaneous photobleaching of both fluorophores in the representative colocalized particle, showing two stepwise changes in fluorescence intensity for hHv1-TFP and TAMRA-C6 (arrows). (*C*) Histogram of photobleaching steps for hHv1-TFP (teal bars) simultaneously photobleached with 1 nM TAMRA-C6 (red bars). Eighty-eight percent of studied particles with hHv1-TFP were bleached in two steps. The data analyzed by the approach of Hines estimate hHv1 channels in surface particles formed with two subunits, with an estimated confidence of >0.999 (*SI Appendix*, Table S2). Among all colocalized particles containing both fluorescent colors, 88% have two TAMRA-C6 bleaching steps at 1 nM TAMRA-C6 (Table 1). (*D*) Titration with increased concentration of TAMRA-C6 onto hHv1-TFP results in increasing fractional colocalized fluorescent particles quantitated using mean MCC. The dose–response is fitted to Hill relationship to obtain a dissociation constant $K_d = 0.75 \pm 0.03$ nM with a Hill coefficient of 1.52 ± 0.13. Each data point represents the mean ± SEM for three to five cells studied in each condition. (*E*) Dose–response for hHv1 titrated with TAMRA-C6 at increasing concentrations was fitted to allosteric Monod–Wyman–Changeux (MWC) model (*Inset*). In the model, the first C6 binds to one subunit of hHv1 with equilibrium association constant K_1. Binding of C6 converts hHv1 subunits from state □ to the ○ state. The second C6 binds to the other subunit with equilibrium association constant K_2. Fitting yields $K_1 = 3.74 \pm 1.12$ nM, $K_2 = 0.31 \pm 0.07$ nM, and gives an allosteric equilibrium constant $L_0 = 9.50 \pm 0.99$. The ratio of K_2/K_1 is 12. When performing nonlinear curve fitting, an adjusted *r*-square value can be obtained for estimating the goodness of fit. The closer the fit is to the data points, the closer *r*-square will be to the value of 1. For fitting with MWC model, an adjusted *r*-square value of 0.9977 was obtained. (*F*) The colocalization of TAMRA-C6 with hHv1 decreases with membrane depolarization. At a RMP of −49.1 ± 3.6 mV, the mean Manders' coefficient of colocalization of TAMRA-C6 was 0.91 ± 0.03 at 10 nM, and this decreased to 0.61 ± 0.06 when 1 nM was applied (Table 1). When the RMP increased to −7.4 ± 0.9 mV (by changing bath KCl), 1 nM TAMRA-C6 yielded a Manders' coefficient of 0.29 ± 0.04, corresponding to an approximately threefold decrease in toxin affinity.

TAMRA-C6 showed a mean Manders' colocalization coefficient (MCC) of 0.11 ± 0.01, indicating ∼11% of hHv1-TFP channels were associated with at least one TAMRA-C6 peptide. As the concentration of TAMRA-C6 was increased, the percentage of particles with both fluorophores increased. At 1 μM TAMRA-C6, colocalization reached a maximum, showing a mean MCC of 0.94 ± 0.02 (Fig. 2*D* and Table 1). A dissociation constant (K_d) of 0.75 ± 0.03 nM and a Hill coefficient of 1.52 ± 0.13 were determined from a fit of the dose–response for colocalization with the following relationship:

$$f = [C6]^h \Big/ \left(K_d{}^h + [C6]^h\right), \qquad [1]$$

where f is the fraction of hHv1-TFP colocalized with TAMRA-C6 at equilibrium, [C6] is the concentration of TAMRA-C6, and h is the Hill coefficient (Fig. 2*D*).

A Hill coefficient of 1.5 is consistent with the idea that two C6 peptides bind to hHv1 channels on two interacting sites (37), a notion supported by the dimeric channel structure and electrophysiology findings supporting energetic coupling of the movement of the two voltage sensors (35, 38, 39). Indeed, fitting the dose–response of hHv1-TFP colocalization with TAMRA-C6 using the Monod–Wyman–Changeux (MWC) model (Eq. **2**) as initially formulated for symmetrically arranged oligomeric proteins of identical subunits, each of which has one binding site for a given ligand (40), the first C6 toxin was estimated to bind with an ∼12-fold lower affinity than a second C6 at two allosterically coupled sites. Thus, when:

$$f = (1 + [C6]/K_2)^n / (L_0(1 + [C6]/K_1)^n + (1 + [C6]/K_2)^n), \qquad [2]$$

where f is the fraction of channels occupied by toxin, [C6] is the concentration of TAMRA-C6 applied, n is the number of sites in channels that can bind toxin, L_0 is the allosteric equilibrium constant, and K_1 and K_2 are the apparent equilibrium association constants for binding of the first and second C6, the MWC model yields a ratio of K_2/K_1 ∼12 (Fig. 2*E*).

Since pixel-by-pixel analysis cannot distinguish between channels with one or two bound toxins, we sought to explicitly assess the stoichiometry of colocalization and to quantify the energetics of cooperativity of C6 binding using single-particle photobleaching (Table 1). Thus, if binding to each channel site was independent, site occupancy would be predicted by a simple, unbiased binomial distribution (41) and the probability (p) of C6 binding to both subunits of hHv1 would follow (Eq. **3**):

$$p = \binom{n}{i} f^i (1-f)^{n-i}, \qquad [3]$$

where f is the fraction of channels with C6 bound, n is the number of binding sites, and i is the number of bound C6. At low [C6] in the case of independence, most channels would have 0 bound toxin and few would have 1 site occupied. In contrast, positive cooperativity that improves binding affinity at a second site would produce channels with two C6 peptides even at low [C6].

When 0.1 nM TAMRA-C6 was applied, only 23 of 200 hHv1-TFP particles confirmed to be intact dimeric channels (because they show two TFP bleaching steps) colocalized with TAMRA-C6 (Table 1). According to independent binding (Eq. **3**), the probability that hHv1 channels carry one C6 ($n = 2, i = 1$) is 20% and two C6 ($n = 2, i = 2$) is 1.3%. In contrast, we observed only 3% of channels with one C6 and 8.5% with two C6 demonstrating binding the first C6 raised the probability for a second C6 binding. Increasing the concentration of TAMRA-C6 to 1 nM, increased the fraction of channels with toxin to 60%, and we still observed only 7% of channels with one C6 bound rather than the 48% predicted by Eq. **3**.

The affinity difference between the two binding events can be estimated from the excess binding of two C6 using Eq. **4**:

Table 1. Parameters of single-molecule photobleaching with hHv1-TFP and TAMRA-C6 by smTIRF

	Subunits expressed and concentrations						
	hHv1-TFP (WT)						
Analysis	0.01 nM TAMRA-C6	0.1 nM TAMRA-C6	1 nM TAMRA-C6	10 nM TAMRA-C6	100 nM TAMRA-C6	1 μM TAMRA-C6	1 nM TAMRA-C6, 100 mM KCl
Manders' coefficient	0.11 ± 0.01	0.14 ± 0.01	0.61 ± 0.06	0.91 ± 0.03	0.93 ± 0.05	0.94 ± 0.02	0.29 ± 0.04
Particles studied							
Total	151	221	114	63	62	125	179
With 2 TFP (dimeric hHv1)	133	200	100	56	55	113	161
With TFP and TAMRA	10	23	60	50	50	105	50
Dimeric hHv1 with one C6	3/133	6/200	7/100	5/56	3/55	8/113	9/161
Dimeric hHv1 with two C6	7/133	17/200	53/100	45/56	44/55	90/113	41/161
Dimeric hHv1 with three C6	0/133	0/200	0/100	0/56	1/55	4/113	0/161
Confidence	0.83	0.98	0.999	0.999	0.999	0.999	0.99
θ	0.89	0.89	0.96	0.96	0.97	0.96	0.96
θ + 1	0.57	0.58	0.64	0.64	0.64	0.64	0.64

hHv1-TFP was expressed in HEK293T cells and incubated with varying concentrations of TAMRA-C6 toxin for reaching equilibrium. Simultaneous, two-color, single-particle photobleaching was studied by TIRF (*Materials and Methods*). Mean Manders' coefficient for colocalization was generated by using unbiased intensity correlation analysis as described in *Materials and Methods*. The number of colocalized particles and photobleaching steps observed for TFP and TAMRA fluorophores in each single fluorescent spot were reported and used for quantitating the cooperative binding of C6. Statistical analysis was performed according to methods described by Hines (*Materials and Methods*). The statistical confidence in the null hypotheses that two TAMRA-C6 bind to hHv1 channel was greater than 0.83. Prebleaching and variance in quantum efficiency reduce the probability of observing each possible bleaching event (θ). θ is calculated from the value of *n* and the distribution of the photobleaching data per Hines. θ is decreased when the distribution is altered to estimate the possibility that higher numbers of missed bleaching steps, for example, θ + 1, indicating that this stoichiometry is less likely. Three TAMRA steps at high concentrations of applied TAMRA-C6 are thought to represent nonspecific or chance association of the third peptide within a diffraction-limited spot.

$$K_{\text{pred}}/K_{\text{obs}} = \left(1-p_{\text{pred}}\right)p_{\text{obs}}\Big/(1-p_{\text{obs}})p_{\text{pred}}, \qquad [4]$$

where p_{pred} is the probability of two bound C6 toxins by Eq. **3**, p_{obs} is the probability of two bound C6 toxins based on observed smTIRF counting, K_{pred} is the dissociation constant predicted without cooperativity, and K_{obs} is the dissociation constant calculated from the observed bias of C6 binding by smTIRF, reflecting the higher affinity of the second site. This yields an affinity difference $K_{\text{pred}}/K_{\text{obs}}$ of approximately sevenfold. The difference in free energy between the two binding events is thus ∼1.2 kcal/mol according to Eq. **5**:

$$\Delta\Delta G = RT\,\ln\left(K_{\text{pre}}/K_{\text{obs}}\right), \qquad [5]$$

where R is the gas constant and T is the temperature in kelvin.

One C6 Binds to Monomeric hHv1 Channels. hHv1 was engineered to suppress formation of dimeric channels by shortening the N terminus and removing the coiled-coil domain at C terminus (*Materials and Methods*); these channels remained operational when truncated and tagged with mTFP1 (ΔhHv1-TFP) (*SI Appendix*, Fig. S1*A*). ΔhHv1-TFP showed one stepwise decrease in fluorescence in 89% of cases consistent with one channel subunit, while 8% of channels were still dimeric (*SI Appendix*, Fig. S1 *A* and *B* and Table S3), as expected (27). With 1 nM TAMRA-C6, 51% of the ΔhHv1-TFP particles colocalized with TAMRA-C6 fluorescence, and bleaching revealed one bound TAMRA-C6 peptide in each case (*SI Appendix*, Fig. S1*B* and Table S3). A fit of the dose–response for ΔhHv1-TFP with TAMRA-C6 according to Eq. **1** offered a K_d of 1.08 ± 0.13 nM and a Hill coefficient of 1.02 ± 0.14 (*SI Appendix*, Fig. S1*C*).

C6 Affinity for hHv1 Decreases with Membrane Depolarization. The affinity of known VSD toxins depends on changes in voltage sensor configuration in response membrane potential (15, 42). To evaluate the influence of potential on C6 binding, we assessed smTIRF colocalization of TAMRA-C6 and hHv1-TFP in HEK293T cells at different resting membrane potential (RMP) by altering extracellular potassium concentration. Cells expressing hHv1 channels had an RMP of −49.1 ± 3.6 mV in bath solution without added KCl and were depolarized to −7.4 ± 0.9 mV by isotonic replacement of 100 mM NaCl with 100 mM KCl. Application of 1 nM TAMRA-C6 under the two conditions showed colocalization with dimeric hHv1-TFP channels to decrease from 61 to 29% with depolarization, yielding a new calculated K_d of ∼2 nM according to Eq. **1**, consistent with an approximately threefold decrease in affinity (Fig. 2*F* and Table 1).

C6 Inhibits hHv1 Proton Currents. HEK293T cells expressing hHv1 generated outward H^+ currents in response to depolarizing steps that we measured using whole-cell patch-clamp recording, and as described by others (6, 43, 44), we observed slow activation and fast deactivation kinetics (Fig. 3*A*). To generate sufficiently large currents to study C6 blockade, hHv1 currents were generated by steps lasting 1.5 s to +40 mV from a holding voltage of −80 mV every 10 s with a 10-fold proton gradient (pH_{in} = 6.5 and pH_o = 7.5). Incubation with 250 nM C6 decreased hHv1 currents ∼45%, and the kinetics of channel activation and deactivation were slowed and speeded by 1.5- and 1.6-fold, respectively (Fig. 3*A*). Consistent with greater affinity for closed states, 250 nM C6 shifted the half-maximal activation voltage ($V_{1/2}$) by +20 mV, and the extent of inhibition was greater at more hyperpolarized potentials (i.e., ∼80% at 0 mV; Fig. 3*B*). C6 blocked hHv1 reversibly with association and dissociation constants determined by single-exponential fits to the time course for block and unblock on acute application and washout of 250 nM C6 (*Materials and Methods*) to yield block parameters of $K_{on} = 3 \times 10^5 \pm 0.8 \times 10^5$/M·s and K_{off} = 0.022 ± 0.001 s^{-1}, respectively (Fig. 3*C*). C6 inhibited hHv1 currents in a dose-dependent manner as expected from smTIRF binding studies. A fit of the dose–response at 40 mV with Eq. **1** yielded a K_i = 30.9 ± 3.4 nM and a Hill coefficient of 0.48 ± 0.04 (Fig. 3*D*).

Supporting the specificity of C6 for hHv1, the proton channel from the sea squirt *Ciona intestinalis*, CiHv1, was insensitive to 1 μM C6 (Fig. 3*D*) despite its homology to hHv1 (44). Similarly,

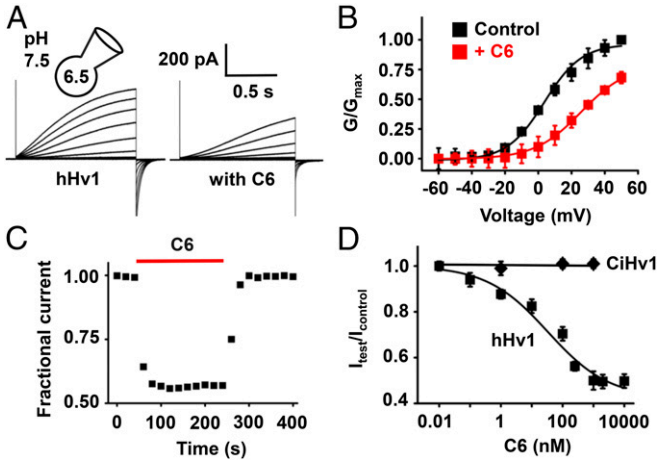

Fig. 3. C6 specifically inhibits hHv1 proton currents. hHv1 and CiHv1 channels were expressed in HEK293T cells and studied by whole-cell patch clamp to assess block parameters using a holding voltage of −80 mV, 1.5-s test pulses, and a 10-s interpulse interval, with $pH_i = 6.5$ and $pH_o = 7.5$. Values are mean ± SEM; $n = 6$–12 cells for each condition. (*A*) Representative proton current traces for hHv1 channels before (*Left*), and in the presence of 250 nM C6 (*Right*) with steps of 10 mV from −80 to 50 mV. The tail current measured immediately following depolarization was used to determine the extent of block. Fitting the activation and deactivation of proton currents at 40 mV to a single exponential function gave time constants τ_{act} of 1,528 ± 116 and 2,183 ± 173 ms, τ_{tail} of 109.2 ± 12.4 and 67.8 ± 9.0 ms without and with C6, respectively. (*B*) Conductance–voltage relationships (*G–V*) for hHv1 (■) in the absence or presence of 250 nM C6 (red, ■). Curves are fitting to the Boltzmann equation. (*C*) The time course for block and unblock of hHv1 on acute application (red bar) and washout of 250 nM C6. Currents were recorded at 40 mV. (*D*) Dose–response relationships for C6 inhibition of hHv1 (■) and CiHv1 (♦). The inhibition constant K_i of C6 for hHv1 channels was estimated from the fit to Eq. **1** and was 30.9 ± 3.4 nM with a Hill coefficient of 0.48 ± 0.04; the maximum inhibition by C6 at +40 mV was 50% of unblocked current. CiHv1 is insensitive to C6 at all tested concentrations up to 1 μM.

1 μM C6 did not inhibit Kv2.1, a channel targeted by a variety of ICK toxins, nor Nav1.4, a channel inhibited by Hm2, the donor of the C domain of C6 (*SI Appendix*, Fig. S2). Consistent with these findings, incubation of 1 μM TAMRA-C6 with cells expressing CiHv1 tagged with mTFP1 (CiHv1-TFP) showed no colocalization using smTIRF studied as in Fig. 2*D* ($n = 100$ channel particles).

C6 Binds to the External S3–S4 Loop of hHv1. Many ICK toxins bind to the S3–S4 loops of VGICs to impede VSD movement. To confirm that the S3–S4 loop of hHv1 provided the binding epitope for C6, we used sites homologous to those Swartz and coworkers (9) had demonstrated allowed transplantation of S3–S4 loops between VGICs to create functional channel chimeras. Indeed, functional channels were produced when the loop residues I183 to L204 (numbered according to hHv1) were transplanted between CiHv1 and hHv1 (Fig. 4*A*). Application of 1 μM C6 to hHv1 carrying the S3–S4 loop of CiHv1 ($Ci_{S3\text{-}S4}$hHv1) showed the channel to be insensitive to the toxin like CiHv1 (Fig. 4*B*). In contrast, transplanting of S3–S4 loop from hHv1 into CiHv1 ($h_{S3\text{-}S4}$CiHv1) conferred C6 toxin sensitivity to the chimera with a K_i of 35 ± 14 nM, a sensitivity like that measured for WT hHv1 under the same study conditions (Fig. 3*D*). Supporting the conclusion that the hHv1 S3–S4 loop is the major binding epitope for C6 in H^+ channels, transplanting of S1–S2 loop of hHv1 into the corresponding region of CiHv1 did not confer C6 toxin sensitivity (*SI Appendix*, Fig. S3) whereas transplanting the S3–S4 loop of hHv1 into the human Kv2.1 potassium channel again conferred inhibition by C6 (*SI Appendix*, Fig. S4).

C6 Blocks the Acrosome Reaction via Inhibition of hHv1 During Capacitation. Human sperm capacitation has been argued to require H^+ efflux via hHv1 to alkalinize the cytoplasm, promoting Ca^{2+} influx via CatSper, and membrane hyperpolarization (Fig. 5*A*) (18, 45). To test this hypothesis, we first sought to confirm that C6 could suppress hHv1 in human sperm. The proton currents were recorded by whole-cell patch clamp in mature human spermatozoa, as described previously (18). As expected, 1 μM C6 slowed proton current activation, speeded deactivation, and decreased H^+ current amplitude with a calculated K_i of 1.0 ± 0.3 μM. In contrast, the control peptide KTx* (16) had no effect on the currents, and as reported by Lishko et al. (18), the current was inhibited by Zn^{2+} ions (Fig. 5*B*).

It is well established that progesterone can trigger the acrosome reaction only in capacitated spermatozoa. Hence, to assess the role of hHv1 in this process, human spermatozoa were incubated under capacitating conditions in the presence of 20 μM KTx* or C6 for 3–4 h. Afterward, the cells were stimulated with progesterone to induce acrosomal exocytosis. While sperm incubated with control peptide reacted normally, showing exocytosis using FITC-coupled *Pisum sativum* agglutinin, those exposed to C6 were inhibited ∼70% (Fig. 5*C*). Inhibition was judged to be on capacitation and not exocytosis because C6 did not suppress when sperm were first capacitated and then incubated for 30 min with peptide before stimulation with progesterone (*SI Appendix*, Fig. S5). C6 did not alter viability nor motility of the sperm, indicating that the effect was not due to peptide toxicity (Fig. 5 *C* and *D*). Moreover, the toxin affected specific aspects of capacitation; for example, it did not alter the tyrosine phosphorylation pattern, a measure of the phosphorylation-signaling pathway crucial to capacitation (*SI Appendix*, Fig. S6).

The proposed role of hHv1 H^+ efflux is to permit Ca^{2+} influx via CatSper, the only channel that mediates Ca^{2+} entry into mature spermatozoa (46–48). In support of this mechanism, 20 μM C6 inhibited the rise in cytoplasmic Ca^{2+} observed with progesterone stimulation using fluorescent Ca^{2+} indicator Fluo-3, while the control peptide had no effect (Fig. 5*E*). To confirm that C6 did not alter Ca^{2+} influx by direct interaction with CatSper, the effect of EGTA on sperm RMP was studied; EGTA chelates extracellular Ca^{2+} promoting Na^+ influx through CatSper resulting in membrane depolarization (49, 50). The same C6 concentration that suppressed the progesterone-induced rise in intracellular Ca^{2+}

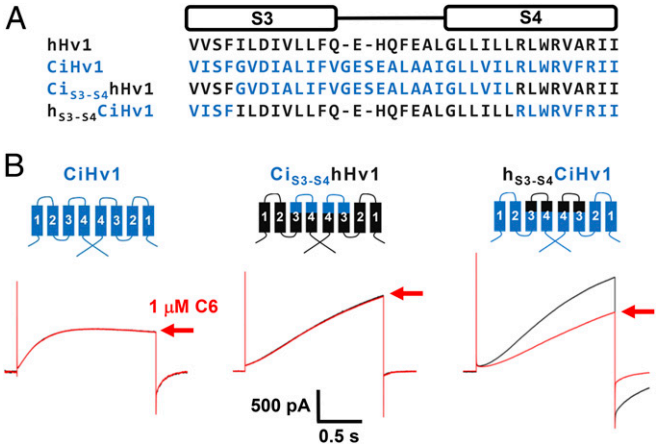

Fig. 4. The S3–S4 loop of hHv1 is the binding epitope for C6. hHv1, CiHv1, and chimera channels were expressed in HEK293T cells and studied as described in Fig. 3. (*A*) Sequence alignments of the S3–S4 motif of hHv1 (black), CiHv1 (blue), and loop transplanting chimeras. The S3–S4 loop of hHv1 or CiHv1 were transplanted into the corresponding region of CiHv1 or hHv1 to produce functional chimeric channels, $h_{S3\text{-}S4}$CiHv1 and $Ci_{S3\text{-}S4}$hHv1, respectively. (*B*) Representative proton current trace for channels (black trace) in the absence or presence of 1 μM C6 (red trace, inhibition at +40 mV after toxin wash-in as indicated by red arrows). *Left*, CiHv1; *Center*, $Ci_{S3\text{-}S4}$hHv1; *Right*, $h_{S3\text{-}S4}$CiHv1. The S3–S4 loop of hHv1 can be transplanted to CiHv1 to confer toxin sensitivity in $h_{S3\text{-}S4}$CiHv1 chimeric channel.

did not alter the EGTA-induced change in RMP, demonstrating that C6 did not block CatSper channel (Fig. 5*F* and *SI Appendix*, Fig. S7).

C6 Inhibits ROS Production in Human WBC. In mouse, mHv1 has been demonstrated to regulate nicotinamide adenine dinucleotide phosphate (NADPH)-dependent oxidase enzymes (NOX) that produce ROS (20, 23). Thus, oxidation of NADPH to $NADP^+$ by NOX is electrogenic, leading to membrane depolarization and cytoplasmic acidification that attenuates production of ROS during the respiratory burst in neutrophils from $mHv1^{-/-}$ mice lacking the channel. Seeking evidence for the same mechanism in human WBCs, we studied H_2O_2 production induced by PMA activation of protein kinase C (PKC) to stimulate respiratory burst using a standard fluorescent assay (20, 21). Consist with expectations, both Zn^{2+} and 1 μM C6 inhibited H_2O_2 production, whereas the effect of control peptide was negligible (Fig. 6*A*). Fitting a dose–response relationship for C6 with Eq. **1** yielded a K_i of 37.2 ± 5.9 nM and a Hill coefficient of 0.63 ± 0.07 (Fig. 6*B*), supporting the conclusion that hHv1 plays an essential role in human WBCs, as mHv1 does in mice, extruding protons during respiratory burst to permit sustained superoxide production.

Discussion

Peptide Toxins Targeting Orphan VSD-Containing Proteins. Venom toxin peptides are among the most powerful tools in the arsenal for the investigation of membrane receptors and are now used as well for diagnosis and treatment of disease (51, 52). Limiting broader use, most receptors of interest lack a recognized peptide that binds with high affinity and specificity. We have previously employed scaffold-based phage-display toxin libraries to produce specific inhibitors that bind in the ion conduction pores of potassium channels. The scorpion α-KTx scaffold was used first to design a library with ~10^4 novel variants and identify Moka1, a toxin with high-affinity and improved specificity for human Kv1.3, which suppresses CD3/28-induced cytokine secretion by T cells without cross-reactive gastrointestinal hyperactivity (16). Subsequently, we constructed a library based on the SAK1 sea anemone toxin scaffold at library diversity of ~10^6 and identified Hui1, a potent and specific inhibitory toxin, and HmK, a potent but promiscuous native toxin, for KcsA, an "orphan" channel without previously known ligands (17). In addition to pore-occluding toxins, voltage-gated channels can be activated or inhibited by gating modifier toxins, which stabilize the VSD in different conformations (11–13). In this work, we create a library with ~10^6 variants based on the ICK toxin scaffold, a backbone found in many natural toxins that target the VSDs of voltage-gated channels. We anticipated that the ICK library would allow selection for peptides that targeted orphan receptors like hHv1 lacking useful regulatory ligands. Here, we describe C6, a de novo toxin containing domains from parental natural toxins in three different species of spiders, isolated by binding of phage to hHv1.

The diverse biological roles of hHv1 make it an important channel to understand and a potential pharmaceutical target. The isolation of C6 for hHv1 using an ICK scaffold (this work), Moka1 for Kv1.3 using an α-KTx scaffold (16), and Hui1 for KcsA on a SAK1 scaffold (17) demonstrates that scaffold-based target-biased libraries and high-throughput phage-display selection allows identification of specific, high-affinity regulators for ion channels targeting their pores and regulatory domains. This supports the notion that other toxin scaffolds should allow ligand selection for other classes of membrane receptors targeted by peptide neurotoxins that are important to human health and disease.

C6 Is an Advanced Tool for Studying hHv1. Indirect evidence has implicated hHv1 in a variety of cellular functions including sperm capacitation, ROS production, and cell proliferation in cancer, but without a known high-affinity and specific ligand confirmation of the roles of the channel and mechanistic inquiry have in some cases been impeded (1). The few reported inhibitors of hHv1, although employed productively, are pharmacologically promiscuous or of low affinity, and include external Zn^{2+} ions (8) and HaTx1, the spider toxin that blocks numerous VGICs including Kv2.1, Kv4.2, Nav1.2, and Cav2.1 (9, 12), and guanidinium derivatives that block from the inside of the membrane (10). C6 has proven to be a valuable tool for studying hHv1 first because it binds to the external VSD loop in hHv1 with a K_d ~1 nM at the natural, hyperpolarized RMP of

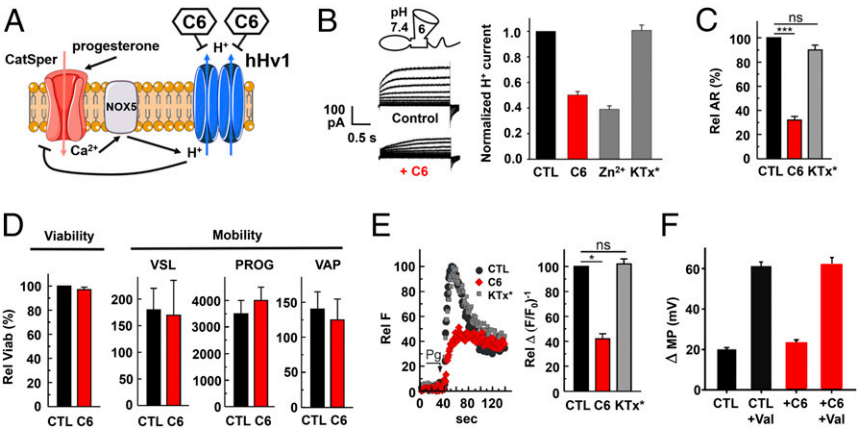

Fig. 5. C6 inhibits hHv1 in human spermatozoa and suppresses the acrosome reaction. As described in *Materials and Methods*, mature human spermatozoa were collected and recorded by whole-cell patch clamp, or studied by light or fluorescent microscopy. In *C–F*, values are mean ± SEM for three separate experiments. (*A*) Schematic representation of synergistic cooperation of hHv1, NOX5, and CatSper in human sperm activation as proposed (54, 62). CatSper is activated by progesterone leading to Ca^{2+} influx. The Ca^{2+}-activated NADPH oxidase 5 (NOX5) catalyzes the translocation of electrons across the plasma membrane, increasing the concentration of H^+ in the cytoplasm. The extrusion of H^+ through hHv1 maintains physiological pH in the cytoplasm. Blocking hHv1 by C6 is predicted to cause cytosolic acidification, decreasing CatSper activity. (*B*) Proton current via hHv1 in human sperm. Representative current traces in response to a test pulse from −80 and 100 mV, in 20-mV increments, in the absence and presence of 1 μM C6 are shown. Inhibition by 1 μM Zn^{2+}, 1 μM C6, and 1 μM control peptide (KTx*) on sperm hHv1 current and measured at the end of the test pulse to 100 mV is plotted. Values are mean ± SEM; $n = 4$ cells for each condition. (*C*) Human spermatozoa were incubated with or without peptides during capacitation, and the acrosome reaction was triggered subsequently by progesterone. After progesterone stimulation, control sperm (black) underwent the acrosome reaction. KTx* (20 μM, gray) did not affect the acrosome reaction, whereas C6 (20 μM, red) caused a ~70% inhibition of the exocytic process. Data were evaluated using Tukey's multiple-comparison posttest for paired comparisons for means. ns, indicates that statistical differences between control and treated samples were nonsignificant ($P > 0.05$), ***$P < 0.001$. (*D*) The viability and motility of sperm were measured for velocity straight line (VSL), progression (PROG), and velocity average path (VAP). Sperm incubated with C6 showed no significant difference in viability or motility. (*E*) Human spermatozoa were incubated with or without peptides during capacitation, and then activated with progesterone, and the increase of cytosolic calcium triggered by progesterone was measured. The relative fluorescence (RF) change with progesterone decreased ~60% in the presence of 20 μM C6. Control peptide KTx* had no effect on calcium signaling, *$P < 0.05$. (*F*) The effect of C6 on CatSper was evaluated by measuring membrane potential change (Δ MP) after adding EGTA to chelate external Ca^{2+} and allow Na^+ to permeate through CatSper, depolarizing the sperm. The ionophore valinomycin shifts the membrane potential of the sperm to the Nernst potential for potassium as previously reported (50). Δ MP represents the difference between membrane potential before and after EGTA addition.

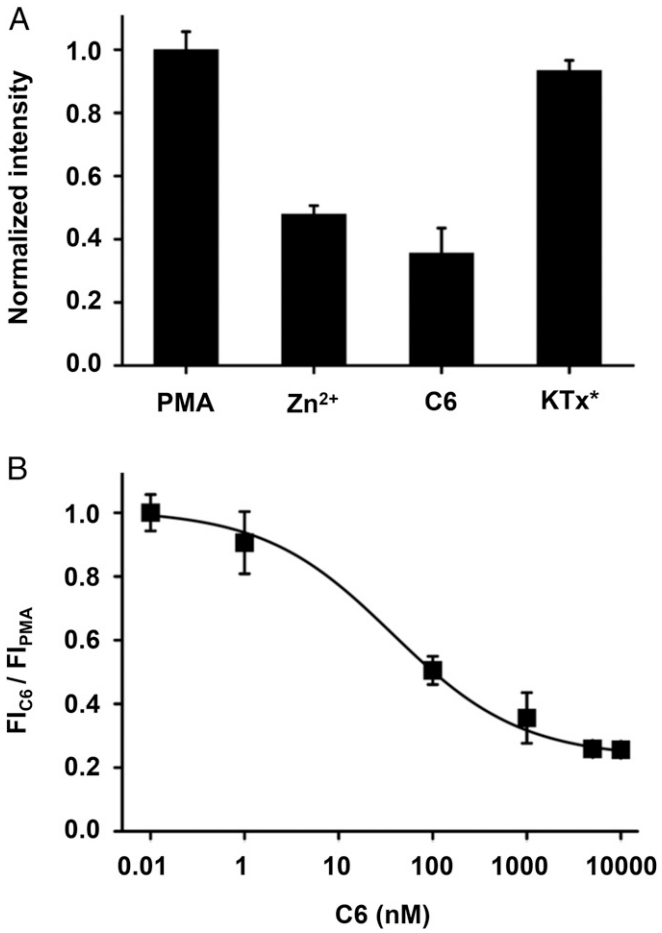

Fig. 6. C6 inhibits ROS production in human WBC during respiratory burst. As described in *Materials and Methods*, H_2O_2 produced by human WBCs in response to PMA was measured spectrophotometrically. Values are mean ± SEM from two independent experiments performed in triplicate. (*A*) H_2O_2 produced 40 min after PMA stimulation. Preincubation with 100 μM Zn^{2+} or 1 μM C6 decreased ROS production, while 10 μM KTx* had no effect. (*B*) Dose–response for C6 inhibition of ROS production fit to Eq. **1** yielded a K_i of 37.2 ± 5.9 nM and a Hill coefficient of 0.63 ± 0.07.

mammalian cells. Second, whereas many ICK toxins modulate more than one VGIC subtype, thus far, C6 appears to be specific to hHv1 since it does not cross-react with exemplar potassium and sodium VGICs (Kv2.1 and Nav1.4), CiHv1, or Catsper in human sperm. As in our prior studies on de novo toxins that target potassium channels, C6 is a third example of achieving target specificity by driving selection for high affinity.

C6 Establishes the Role of hHv1 on Capacitation of Human Sperm. Capacitation is a requirement for sperm to undergo the acrosomal reaction and to develop hyperactivated motility, two necessary conditions for fertilizing an egg (53). It is hypothesized that hHv1, the Ca^{2+}-activated enzyme NOX5, and CatSper form a synergistic network in the human sperm plasma membrane that regulates intracellular pH, redox potential, and cytosolic free Ca^{2+} concentration, which are all crucial for sperm capacitation (2). Lishko et al. (18) presented strong evidence that sperm function depends on proton efflux via hHv1 to induce intracellular alkalization using nonspecific inhibitors like Zn^{2+}, noting however that this role for hHv1 could not be confirmed without a reagent that specifically blocks the channel. Moreover, the model for human sperm cannot be supported using $mHv1^{-/-}$ mice since they are fertile indicating that a different mechanism is operating in this species (20, 23, 24). Here, we employed C6 to study human sperm to show that the activity of hHv1 channels is necessary during capacitation to allow the intracellular calcium rise and acrosomal reaction stimulated by a physiological inducer for fertilization, as proposed by Lishko et al. (18).

C6 Confirms the Role of hHv1 Role in ROS Production by Human WBCs. Oxidation of NADPH to $NADP^+$ by NOX enzymes transports electrons across the cell membrane to reduce oxygen to superoxide, with subsequent conversion to H_2O_2, a process essential to innate immunity (54). This physiological process of ROS production leads to membrane depolarization and intracellular acidification (24, 55). To sustain the cascade in mice, mHv1 is required to extrude protons to maintain cytoplasmic pH in the physiological range and contribute to membrane repolarization, a mechanism confirmed using a knockout strategy (20, 23, 24). Here, we demonstrate the required role for hHv1 operation in human WBCs, using C6 to suppress high-level superoxide production during the respiratory burst induced by PMA.

C6 Inhibition, a Cooperative Voltage-Dependent Mechanism. The affinity of C6 for hHv1 decreases with depolarization. At −50 mV, smTIRF shows that incubation of HEK293T cells with 1 nM C6 yields 53% of hHv1 channels with two bound toxins, 7% with one toxin, and 40% with no toxin (Table 1), indicating a K_D of 0.75 nM and positive cooperativity of toxin binding to the closed channel state. After a step lasting 1.5 s to 40 mV, the K_D increases 40-fold to 30 nM as judged by current inhibition, and blockade is partial, reaching just 50% with 1 μM C6 in the bath (Fig. 3*D*). These observations are consistent with the action of ICK toxins that alter VGIC gating by binding to VSDs described by the research groups of Bezanilla (56), Swartz (42), and Catterall (57) where the outward movement of the S4 segment accelerates the dissociation of the toxins from their target sites and thus binding affinity correlates closely with the membrane potential and gating states of VGICs (13). As seen with other gating modifier toxins that bind with greater affinity to closed channels, C6 slows the channel activation, speeds deactivation, and shifts the voltage dependence of activation to more positive potentials. Our results, and the operation of other gating-modifying toxins, point to a model in which C6 binding to hHv1 is favored in the "down" conformation of the VSD.

We have shown that hHv1 has two C6 binding sites, one on the S3–S4 loop of each subunit, and that the binding of the first C6 increases the affinity of the second site for C6. Because monomeric ΔhHv1 channels are able to bind one C6 without evidence of an allosteric effect, the positive cooperativity for binding to dimeric hHv1 channels represents either attraction between the two peptides or, as we suspect, intrinsic cooperativity of gating between two subunits of the hHv1. Thus, attaching a fluorophore to the S4 segments of hHv1 channels (altered to open more readily) has demonstrated that movement of one voltage sensor in hHv1 accelerates the movement of the other such that the two pores tend to be in the same state, open or closed (38). Therefore, we favor the idea that binding the first C6 favors the closed state of both its own VSD receptor and the *trans* site on the other subunit, improving the energetic favorability of the second binding reaction (by ∼1.2 kcal/mol in HEK293T cells as studied for smTIRF). Similarly, we interpret the apparent negative cooperativity for C6 inhibition at +40 mV to reflect coupled opening of the two pores at the positive membrane potential, favoring dissociation of the second C6 once the first toxin has left its site.

Tombola et al. (38) reported that the two hHv1 subunits in dimeric channels (mutated to activate at more hyperpolarized potentials than WT) show intersubunit interactions so robust that the second subunit was ∼60 times more likely to open when the other subunit was already open. Subsequently, Tombola and coworkers (58) found that the 2-guanidinothiazole derivative GBTA inhibited open hHv1 channels by binding cooperatively in the intracellular cavities of both subunits at +120 mV, interpreting the binding of GBTA to one subunit to increase in binding affinity of the neighboring subunit with a difference

between the binding free energies of the lowest affinity and highest affinity sites of ~1.3 kcal/mol, similar to the cooperativity of external C6 binding we estimate by smTIRF to closed dimeric hHv1 channels at approximately −50 mV (~1.2 kcal/mol). These findings each reflect cooperativity of the closed and the open states of the two subunits in hHv1.

The mechanism of voltage-dependent C6 blockade of hHv1 merits further elucidation, for example, to compare it with the action of native ICK toxins on VGIC (42) and, particularly, as it relates to inhibition of the proton channels as they operate in sperm and WBCs because the membrane potentials of the native cells change with activity. At baseline, the RMP of human sperm is −40 mV and it drops to −60 mV with capacitation (45), thus remaining hyperpolarized at potentials where C6 is expected to block with high affinity and positive cooperativity. In contrast, the RMP of neutrophils is estimated to be −60 mV and it rises to 60 mV on activation (59), indicating that C6 blockade will be more effective before NADPH oxidase activity increases during respiratory burst, depolarizing the cells, diminishing the affinity of C6 for hHv1 channels.

Materials and Methods

Library Construction and Screening. The sequence of natural spider toxin ProTx-II was used as a template for selecting 110 parent toxins sequences from a BLAST search of the UniProt database as previously described (17, 60). Sequences were aligned based on the six conserved cysteine residues that form disulfide bridges and the ICK scaffold. Three domains were defined by the second and fifth conserved cysteine, allowing for insertions and deletions, and 110 ICK scaffold toxins give 95, 104, and 106 unique A, B, and C domains, respectively. Nucleotide duplexes encoding the second and fifth cysteine were ligated unidirectionally to produce toxin genes with only the correct domain order. Separate reactions were preformed to ligate the gene inserts into pAS62 in frame with M13 filamentous phage particle coat protein pIII. Ligation mixtures were transformed into SS320 electrocompetent cells and sequencing of 376 plaques confirmed unbiased insert utilization. Library phages and single toxin phages were prepared as previously described (16).

hHv1 protein (hHv1-VSD, residues 75–223) was purified as previously described (27). hHv1 protein was biotinylated using sulfosuccinimidyl 2-(biotinamido)-ethyl-1,3-dithiopropionate (EZ-Link Sulfo-NHS-SS-Biotin; Thermo Scientific). Biotinylation was verified by a pull-down assay using streptavidin MagneSphere beads (Promega). The 500 nM biotinylated hHv1 protein was adsorbed to 100-μL streptavidin MagneSphere paramagnetic particles, and free streptavidin-binding sites were blocked with biotin to prevent nonspecific binding. Beads were washed four times with TBS (25 mM Tris·HCl, 140 mM NaCl, and 3 mM KCl, pH 7.4) containing 0.1% Tween 20, 1% BSA, and 2 mM 1-palmitoyl-2-hydroxy-*sn*-glycero-3-phosphate-(1′-rac-glycerol) (LPPG) (Avanti Polar Lipids) (TBSTBL). Phage expressing the toxin library diluted to 10^{10} pfu in 100 μL of TBS containing 0.5% BSA and 2 mM LPPG and mixed with hHv1 protein adsorbed Magnesphere beads and allowed to bind for 1 h at room temperature. A KingFisher (Thermo Fisher Scientific) automated magnetic bead manipulator was used to wash the beads three to five times with TBSTBL, so that the poorly adherent phage particles were removed. Tightly bound phage was detached from the beads using 100 mM DTT. The supernatant was collected and used to infect log-phase *Escherichia coli* XL-1 blue (Stratagene) immediately. Infected *E. coli* were used for quantification by titering and for phage amplification.

Alternative rounds of panning were done with NUNC-Immuno MaxiSorp 96-well plates (Thermo Fisher Scientific) that were coated overnight at 4 °C with 100 mM $NaHCO_3$ and 1 μg/well hHv1 protein to decrease nonspecific phage enrichment. Wells were washed twice with TBSTBL and then blocked with TBS containing 1% BSA and 0.2% Tween 20 (TBSTB) overnight at 4 °C. Wells were washed twice more with TBSTB. Library phage was dilute to 10^{10} pfu/mL in TBSTBL and added to the wells. Phages were allowed to bind for 1 h at room temperature. Poorly adherent phage was removed by washing three to five times with TBSTBL manually. Bound phages were eluted with 100 μL of 0.1 M triethylamine by incubation for 10 min on a rocking shaker. The pH of the eluate was adjusted to between 7.0 and 8.5 with 1 M Tris·HCl (pH 8.0). Amplification and titering of phage was done in the same way as described above. After five rounds of library sorting (three rounds using MagneSphere with adsorbed biotinylated hHv1 protein, and two rounds using NUNC-Immuno plates directly coated with hHv1 protein as target), 44 clones were genotyped by DNA sequencing to confirm enrichment.

Toxin Synthesis and Fluorescent Labeling. C6 toxin (MH828728) was purchased as synthetic peptides from CSBio. Peptide toxin folding reactions were quenched by acidification and purified by reverse-phase HPLC as before. Peptides that were more than 95% pure were lyophilized and stored at −20 °C. Peptides were dissolved in appropriate external solutions for whole-cell patch-clamp recordings or physiological assays before use.

C6 peptide was labeled with 5-(and-6-)-carboxytetramethyl-rhodamine succinimidyl ester (5,6-TAMRA-SE) (Life Technologies). C6 was dissolved in 50 mM Hepes, 100 mM NaCl at pH 7.5 to 5 mg/mL concentration. 5,6-TAMRA-SE dye was dissolved in 500 μL of DMSO per manufacturer instructions. C6 and dye were mixed at a ratio of 1:10 for 1 h at room temperature on a rotating shaker. The labeled C6 was purified by HPLC over a 20–50% acetonitrile gradient and the corresponding single peak was collected. Samples were lyophilized and stored at −80 °C. Labeled peptide was dissolved in appropriate external solution before use.

Molecular Biology. Human Hv1 (NM_001040107) or *Ciona intestinalis* Hv1 (NM_001078469) tagged with a TFP connected by a 13-residue flexible linker were constructed using gBlock gene fragments (Integrated DNA Technologies) and inserted into a laboratory dual-purpose vector pMAX+ using Gibson Assembly (New England BioLabs). Monomeric human ΔHv1 was constructed by truncating hHv1 subunit at position 82 for N terminus and 219 for C terminus and was tagged with TFP identically to WT and inserted into pMAX+. $h_{S3\text{-}S4}$CiHv1 was constructed by replacing the S3–S4 loop (G231–L254) of CiHv1 with S3–S4 loop (I183–L204) of hHv1. $Ci_{S3\text{-}S4}$Hv1 was constructed by replacing the S3–S4 loop (I183–L204) of hHv1 with S3–S4 loop (G231–L254) of CiHv1. $h_{S1\text{-}S2}$CiHv1 was constructed by replacing the S1–S2 loop (L169–L187) of CiHv1 with S1–S2 loop (I121–F139) of hHv1. $h_{S3\text{-}S4}$Kv2.1 was constructed by replacing the S3–S4 loop (V275–L305) of hKv2.1 with S3–S4 loop (I183–W207) of hHv1. All chimeras were assembled into pMAX+ using Gibson assembly (Integrated DNA Technologies). $rNa_v1.4$ (NP_037310) carried in vector pcDNA1 and hKv2.1 (NP_004966) in pMAX+ were used as previously described.

Cell Culture. HEK293T cells were purchased from ATCC and maintained in DMEM (ATCC) supplemented with 10% FBS and 1% penicillin and streptomycin. Plasmids were transfected into cells using Lipofectamine 2000 (Life Technologies) according to the manufacturer's instructions. Experiments were performed 24–48 h posttransfection.

Two-Color smTIRF for Photobleaching and Analysis of Fluorescence Colocalization and hHv1 Subunit Stoichiometry. HEK293T cells were seeded on glass-bottom dishes (Chemglass Life Science) and transfected with hHv1-TFP as described above. The surface density of channel molecules was kept <200 in 10 × 10-μm field for minimizing the overlapping of multiple channels within a diffraction-limited spot. TAMRA-C6 was added in 100 mM Hepes, 100 mM NaCl, 0.5 mM $CaCl_2$, 1.2 mM $MgCl_2$, and 10 mM glucose, pH 7.5, to the dishes and incubated adequate times for reaching binding equilibrium. Cells were extensively washed to remove nonspecifically bound toxins before recording. Single protein molecules or complexes at the surface of live HEK293T cells were identified by using TIRF microscope as described (31).

Critical angle for TIRF was adjusted using a CellTIRF illuminator (Olympus) and a high numerical aperture apochromat objective (150×, 1.45 N.A.) mounted on an automated fluorescence microscope controlled by Metamorph software (Molecular Devices). CellTIRF software (Olympus) was used to simultaneously illuminate both fluorophores at a critical angle such that only 100 nm deep was illuminated. TAMRA was excited with the 561-nm laser line and TFP was excited at a 445-nm laser line. Emitted light signals were split with a 520-nm dichroic mirror mounted in a DualView adapter (Photometrics), which allows each wavelength to be directed to one-half of a back-illuminated EM-CCD. Stoichiometry was assessed by simultaneous photobleaching with continual excitation. Data were captured as movies of 100–370 frames acquired at 1 Hz. Data were analyzed as previously described. When TAMRA was with TFP in the same cell, the data for each fluorophore were saved as separate stacks and processed in an identical manner. The Manders' coefficient of colocalization between fluorophores was determined by unbiased intensity correlation analysis using the Coloc2 plugin in ImageJ to confirm overlap of the two molecules. Fluorescence measured from each region was plotted versus time to determine the number of bleaching steps at each point.

Statistical analyses to calculate estimated confidence with which stoichiometry could be inferred from the observed data and θ, the probability of successfully observing each possible photobleaching event, were performed in R Studio, based on methods developed by Hines (36). The densities of colocalized and single fluorescent spots were determined following thresholding and watershed separation in ImageJ. Then, the particle number was

counted in separate regions of interest for three to five cells per group by using the Analyze particles plugin.

Electrophysiology. Proton current from hHv1, CiHv1, and chimera channels were recorded in whole-cell mode using an Axopatch 200B amplifier. Stimulation and data collection were done with a Digidata1322A and pCLAMP 9 and 10 software (Molecular Devices). Cells were perfused with an external solution of 100 mM Hepes, 100 mM NaCl, and 10 mM glucose at pH 7.5. Pipettes with resistances between 3 and 5 MΩ were filled with 100 mM Bis-Tris buffer, 100 mM NaCl, and 10 mM glucose at pH 6.5. Capacitance was subtracted online. Sampling frequency was 10 kHz and was filtered at 1 kHz. C6 was applied in 100 mM Hepes, 100 mM NaCl, 10 mM glucose, with 0.05% fatty acid-free BSA (Sigma) at pH 7.5, and effects were monitored by protocols evoking current by stepping to 40 mV for 1.5 s from a holding voltage of −80 mV, with 10 s between any given pulse. Current–voltage relationships were evoked from a holding potential of −80 mV to test pulses from −80 to 50 mV for 1.5 s in 20-mV intervals every 10 s. Fractional unblocked current was assessed at the end of the test pulse or immediately after repolarization. The conductance–voltage relationships were determined as described by DeCoursey in ref. 61, the reversal potential (V_{rev}) is calculated with the equation $V_{rev} = (I_{end} - I_{tail})/(V_{test} - V_{hold})$ and were fit to the Boltzmann equation, $G = G_{max}/[1 + \exp(-zF(V - V_{1/2})/RT)]$, where V is the test potential, $V_{1/2}$ is the voltage of half-maximal activation, z is the effective valence, T is the temperature, R is the gas constant, and F is the Faraday constant. Deactivation kinetics for Hv1 with and without C6 were determined by fitting traces with single-exponential functions. Activation kinetics were fit with a single exponential with a delay. k_{on} and k_{off} were estimated from fits of the kinetics of toxin wash-in and wash-out and calculated using the following equations:

$$\tau_{on} = (k_{on}[\mathrm{Tx}] + k_{off})^{-1}, \quad [6]$$

and

$$\tau_{off} = (k_{off})^{-1}. \quad [7]$$

A dose–response curve was determined by plotting the fractional unblocked current, $I_{C6}/I_{control}$, versus concentration of C6. Dose–response curve was fit with Hill equation in Origin 8.0.

Perforated patch clamp was performed with nystatin (Sigma) at 150 μg/mL in the pipette solution. After seal formation, the RMP of cells expressing hHv1 channels was measured in current-clamp configuration after attainment of whole-cell configuration with 10 mM Hepes, 136 mM KCl, 1 mM $MgCl_2$, 2 mM K_2ATP, 5 mM EGTA, pH 7.2 in the pipette and the bath solution described in *Two-Color smTIRF for Photobleaching and Analysis of Fluorescence Colocalization and hHv1 Subunit Stoichiometry*.

Xenopus laevis oocytes were injected with cRNA encoding hKv2.1 or $h_{S3\text{-}S4}$Kv2.1. Recording solution was as follows (in mM): 50 KCl, 50 NaCl, 1 $MgCl_2$, 0.3 $CaCl_2$, 10 Hepes, pH 7.5, with 0.05% BSA (fraction V; Fisher Scientific). Recordings were performed with constant gravity flow of solution at 2 mL/min yielding chamber exchange in ∼5 s. Currents were recorded 1–3 d after cRNA injection using an Oocyte clamp amplifier OC-725C (Warner Instruments), and electrodes were filled with 3 M KCl with resistance of 0.3–1 MΩ. Data were filtered at 1 kHz and digitized at 20 kHz using pClamp software and assessed with Clampfit v9.0 and Origin 8.0.

Sperm Electrophysiology and Membrane Potential Measurements. Procedures were approved by the Bioethics Committee at the Biotechnology Institute from the National Autonomous University of Mexico. All semen donors gave written informed consent. Ejaculates were obtained from healthy donors by masturbation after at least 48 h of sexual abstinence. Only semen samples that fulfilled the World Health Organization 2010 guidelines were selected for experiments. Motile sperm were recovered after a swim-up separation for 1 h in modified Krebs–Ringer bicarbonate medium under noncapacitation conditions (without BSA and Ca^{2+}) at 37 °C in a humidified atmosphere of 5% CO_2–95% air. Spermatozoa were stored in physiological solution comprising the following (in mM): 135 NaCl, 5 KCl, 1 $MgSO_4$, 2 $CaCl_2$, 5 glucose, 1 sodium pyruvate, 10 lactose, and 20 Hepes (pH 7.4) until used in electrophysiological recordings.

Whole-cell patch clamp was used for recording proton currents sealing at the cytoplasmic droplet from mature human spermatozoa plated on poly-lysine–coated coverslips. Pipettes (20–30 MΩ) were filled with the following: 135 mM *N*-methyl-D-glucamine (NMDG), 5 mM ethylene glycol tetraacetic acid (EGTA), and 100 mM Mes (pH 6.0) with methanesulfonic acid (CH_3SO_3H). Seals between the patch pipette and the sperm cytoplasmic droplet were formed in physiological solution. After transition into whole-cell mode, the bath solution was changed for proton current recording (in mM): 130 NMDG, 1 EDTA, and 100 Hepes (pH 7.4) with CH_3SO_3H. Pulse protocol application and data acquisition were performed with a patch-clamp amplifier (Axopatch 200; Molecular Devices) and using the pCLAMP6 software (Molecular Devices). Data were sampled at 2–5 kHz and filtered at 1 kHz and were analyzed with Clampfit 10.6 (Molecular Devices) and SigmaPlot 9.0 (Systat Software). Data were calculated and plotted as the mean ± SEM, and $n = 4$. All electrophysiological recordings were performed at 23 °C.

Mature sperm were collected and diluted in noncapacitating medium, and exposed to 1 μM Dis-C3-(5). After adding 3.5 mM EGTA, which chelates external Ca^{2+} and allows Na^+ to pass through Catsper channels, fluorescence (620/670 nm excitation/emission) was recorded continuously, as previously described (50). Calibration was performed by supplementing with 1 μM valinomycin and with sequential additions of KCl.

Sperm Physiology and Biochemistry. Human semen samples were provided by masturbation from healthy volunteer donors. The informed consent signed by the donors and the protocol for semen sample handling were approved by the Ethics Committee of the School of Medicine, National University of Cuyo. After sample liquefaction (20–30 min at 37 °C), highly motile sperm were recovered by swim-up separation for 1 h in human tubal fluid media (HTF) (as formulated by Irvine Scientific) supplemented with 5 mg/mL BSA at 37 °C in an atmosphere of 5% CO_2/95% air. Sperm suspensions were diluted to 10^7 sperm/mL with HTF-BSA and incubated 3–4 h in the presence or absence of peptides under conditions that promote capacitation. After this incubation, sperm physiology was assessed by different assays.

Acrosome reaction. Sperm were incubated for 30 min at 37 °C with 15 μM progesterone, spotted on slides, air-dried, and stained with FITC-coupled *Pisum sativum* agglutinin (FITC-PSA) (25 μg/mL in PBS) for 40 min at room temperature. For some experiments, before stimulation with progesterone, sperm were first capacitated and then incubated for 30 min with the peptides. The presence of an intact acrosome was assessed in at least 200 cells per condition using an upright Nikon Optiphot II microscope equipped with epifluorescence optics. Acrosome reaction was expressed as a percentage of the stimulation observed in sperm incubated in the absence of toxins (control, 100%).

Tyrosine phosphorylation. Sperm were lysed and proteins were separated on Tris-tricine-SDS gels and transferred to 0.45-μm nitrocellulose membranes (Hybond; GE Healthcare). Nonspecific reactivity was blocked by incubation for 1 h at room temperature with 5% (wt/vol) BSA dissolved in washing buffer (PBS with 0.2% Tween 20, pH 7.6). Blots were incubated with the anti-phosphotyrosine, or anti–α-tubulin antibodies in blocking solution for 1 h at room temperature. HRP-conjugated goat anti-mouse IgGs were used as secondary antibodies with 1-h incubations. Excess of first and second antibodies was removed by washing five times for 10 min each in washing buffer. Detection was performed with a Millipore chemiluminescence system and a Fujifilm LAS-4000 Luminescent Image Analyzer. Quantification of signal intensities was performed with ImageJ software.

Viability and motility measurements. Capacitated sperm were observed in bright field using a Nikon TE300 microscope. One-minute videos were obtained and analyzed with ImageJ software and CASA plugin for measuring motility parameters.

Intracellular Ca^{2+} measurements. Sperm were incubated with 2 μM Fluo-3 AM (Invitrogen) in the dark at 37 °C during 30 min. Cells were washed once with human sperm medium (HSM) with the following (in mM): 120 NaCl, 4 KCl, 2 $CaCl_2$, 15 $NaHCO_3$, 1 $MgCl_2$, 10 Hepes, 5 D-glucose, 1 sodium pyruvate, and 10 L-(+)-lactate acid adjusted to pH 7.4 and placed in 300-μL cuvette with continuous stirring. Fluorescence intensity was measured with an Aminco Bowman II spectrofluorimeter (λ_{Ex} = 506, λ_{Em} = 526). Data were collected during 350 s at a frequency of 0.5 Hz. The raw intensity values were normalized as $[(F/Fo)^{-1}]$, where F is fluorescence intensity at time t and Fo is the mean of F taken during the control period. The resulting values were expressed as relative fluorescence (RF) normalized to the maximum fluorescence obtained after the TX-100 addition. Statistical analyses were performed using Tukey's multiple-comparison posttest. Results were considered significantly different at $P < 0.05$.

ROS Assay. Single-donor human whole blood was purchased from Innovative Research. The protocol for blood sample handling was approved by the Institutional Biosafety Committee at Brandeis University. Blood was used within 48 h of sampling and stored at 4 °C with K_2 EDTA as an anticoagulant until use. Upon arrival, cells were counted and diluted to 5×10^6 cells per mL in Tyrode's solution (TS) (Sigma). A volume of 180 μL of a buffer solution containing 100 μM Amplex Red (Life Technologies) and 0.5 units/mL HRP in

TS was added to each well in a 96-well plate. Diluted blood (20 μL) was added to each well. $ZnCl_2$ (100 μM), KTx* (10 μM), or various concentrations of C6 were added to selected wells in triplicate. Plates were incubated at 37 °C for 1 h. PMA (200 nM) (Sigma) was added to selected wells, and fluorescence was recorded immediately at 530/590 nm (excitation/emission). Fluorescence was recorded every 10 min for 1 h after PMA addition.

ACKNOWLEDGMENTS. We are grateful for grant support from the NIH [GM111716 (to S.A.N.G.) and GM57846 (to E.P.)]; the US–Israel Binational Science Foundation (BSF 2017243) (to S.A.N.G.); Universidad Nacional de Cuyo, Argentina (06/J388) (to L.S.M.); Consejo Nacional de Investigaciones Científicas y Técnicas, Argentina (PIP 112-200801-02277) (to L.S.M.); and Agencia Nacional de Promoción Científica y Tecnológica, Argentina (PICT-2011-2310) (to L.S.M.).

1. DeCoursey TE (2013) Voltage-gated proton channels: Molecular biology, physiology, and pathophysiology of the H_V family. *Physiol Rev* 93:599–652.
2. Lishko PV, et al. (2012) The control of male fertility by spermatozoan ion channels. *Annu Rev Physiol* 74:453–475.
3. Demaurex N, El Chemaly A (2010) Physiological roles of voltage-gated proton channels in leukocytes. *J Physiol* 588:4659–4665.
4. Tombola F, Ulbrich MH, Isacoff EY (2009) Architecture and gating of Hv1 proton channels. *J Physiol* 587:5325–5329.
5. Okamura Y, Fujiwara Y, Sakata S (2015) Gating mechanisms of voltage-gated proton channels. *Annu Rev Biochem* 84:685–709.
6. Ramsey IS, Moran MM, Chong JA, Clapham DE (2006) A voltage-gated proton-selective channel lacking the pore domain. *Nature* 440:1213–1216.
7. Musset B, et al. (2011) Aspartate 112 is the selectivity filter of the human voltage-gated proton channel. *Nature* 480:273–277.
8. Cherny VV, DeCoursey TE (1999) pH-dependent inhibition of voltage-gated H^+ currents in rat alveolar epithelial cells by Zn^{2+} and other divalent cations. *J Gen Physiol* 114:819–838.
9. Alabi AA, Bahamonde MI, Jung HJ, Kim JI, Swartz KJ (2007) Portability of paddle motif function and pharmacology in voltage sensors. *Nature* 450:370–375.
10. Hong L, Pathak MM, Kim IH, Ta D, Tombola F (2013) Voltage-sensing domain of voltage-gated proton channel Hv1 shares mechanism of block with pore domains. *Neuron* 77:274–287.
11. Swartz KJ (2007) Tarantula toxins interacting with voltage sensors in potassium channels. *Toxicon* 49:213–230.
12. Bosmans F, Swartz KJ (2010) Targeting voltage sensors in sodium channels with spider toxins. *Trends Pharmacol Sci* 31:175–182.
13. Catterall WA, et al. (2007) Voltage-gated ion channels and gating modifier toxins. *Toxicon* 49:124–141.
14. Lee HC, Wang JM, Swartz KJ (2003) Interaction between extracellular Hanatoxin and the resting conformation of the voltage-sensor paddle in Kv channels. *Neuron* 40:527–536.
15. Cestèle S, et al. (1998) Voltage sensor-trapping: Enhanced activation of sodium channels by beta-scorpion toxin bound to the S3-S4 loop in domain II. *Neuron* 21:919–931.
16. Takacs Z, et al. (2009) A designer ligand specific for Kv1.3 channels from a scorpion neurotoxin-based library. *Proc Natl Acad Sci USA* 106:22211–22216.
17. Zhao R, et al. (2015) Designer and natural peptide toxin blockers of the KcsA potassium channel identified by phage display. *Proc Natl Acad Sci USA* 112:E7013–E7021.
18. Lishko PV, Botchkina IL, Fedorenko A, Kirichok Y (2010) Acid extrusion from human spermatozoa is mediated by flagellar voltage-gated proton channel. *Cell* 140:327–337.
19. DeCoursey TE, Morgan D, Cherny VV (2003) The voltage dependence of NADPH oxidase reveals why phagocytes need proton channels. *Nature* 422:531–534.
20. Ramsey IS, Ruchti E, Kaczmarek JS, Clapham DE (2009) Hv1 proton channels are required for high-level NADPH oxidase-dependent superoxide production during the phagocyte respiratory burst. *Proc Natl Acad Sci USA* 106:7642–7647.
21. El Chemaly A, et al. (2010) VSOP/Hv1 proton channels sustain calcium entry, neutrophil migration, and superoxide production by limiting cell depolarization and acidification. *J Exp Med* 207:129–139.
22. Lishko PV, Kirichok Y (2010) The role of Hv1 and CatSper channels in sperm activation. *J Physiol* 588:4667–4672.
23. Okochi Y, Sasaki M, Iwasaki H, Okamura Y (2009) Voltage-gated proton channel is expressed on phagosomes. *Biochem Biophys Res Commun* 382:274–279.
24. Morgan D, et al. (2009) Voltage-gated proton channels maintain pH in human neutrophils during phagocytosis. *Proc Natl Acad Sci USA* 106:18022–18027.
25. Schmalhofer WA, et al. (2008) ProTx-II, a selective inhibitor of NaV1.7 sodium channels, blocks action potential propagation in nociceptors. *Mol Pharmacol* 74:1476–1484.
26. Daly NL, Craik DJ (2011) Bioactive cystine knot proteins. *Curr Opin Chem Biol* 15:362–368.
27. Li Q, et al. (2015) Resting state of the human proton channel dimer in a lipid bilayer. *Proc Natl Acad Sci USA* 112:E5926–E5935.
28. Chong Y, et al. (2007) The omega-atracotoxins: Selective blockers of insect M-LVA and HVA calcium channels. *Biochem Pharmacol* 74:623–638.
29. Liao Z, et al. (2007) Proteomic and peptidomic analysis of the venom from Chinese tarantula *Chilobrachys jingzhao*. *Proteomics* 7:1892–1907.
30. Billen B, Vassilevski A, Nikolsky A, Tytgat J, Grishin E (2008) Two novel sodium channel inhibitors from Heriaeus melloteei spider venom differentially interacting with mammalian channel's isoforms. *Toxicon* 52:309–317.
31. Plant LD, Xiong D, Dai H, Goldstein SA (2014) Individual IKs channels at the surface of mammalian cells contain two KCNE1 accessory subunits. *Proc Natl Acad Sci USA* 111: E1438–E1446.
32. Plant LD, Marks JD, Goldstein SA (2016) SUMOylation of $Na_V1.2$ channels mediates the early response to acute hypoxia in central neurons. *eLife* 5:e20054.
33. Xiong D, et al. (2017) SUMOylation determines the voltage required to activate cardiac IKs channels. *Proc Natl Acad Sci USA* 114:E6686–E6694.
34. Koch HP, et al. (2008) Multimeric nature of voltage-gated proton channels. *Proc Natl Acad Sci USA* 105:9111–9116.
35. Tombola F, Ulbrich MH, Isacoff EY (2008) The voltage-gated proton channel Hv1 has two pores, each controlled by one voltage sensor. *Neuron* 58:546–556.
36. Hines KE (2013) Inferring subunit stoichiometry from single molecule photobleaching. *J Gen Physiol* 141:737–746.
37. Prinz H (2010) Hill coefficients, dose-response curves and allosteric mechanisms. *J Chem Biol* 3:37–44.
38. Tombola F, Ulbrich MH, Kohout SC, Isacoff EY (2010) The opening of the two pores of the Hv1 voltage-gated proton channel is tuned by cooperativity. *Nat Struct Mol Biol* 17:44–50.
39. Lee SY, Letts JA, Mackinnon R (2008) Dimeric subunit stoichiometry of the human voltage-dependent proton channel Hv1. *Proc Natl Acad Sci USA* 105:7692–7695.
40. Monod J, Wyman J, Changeux JP (1965) On the nature of allosteric transitions: A plausible model. *J Mol Biol* 12:88–118.
41. MacKinnon R (1991) Determination of the subunit stoichiometry of a voltage-activated potassium channel. *Nature* 350:232–235.
42. Phillips LR, et al. (2005) Voltage-sensor activation with a tarantula toxin as cargo. *Nature* 436:857–860.
43. Musset B, et al. (2008) Detailed comparison of expressed and native voltage-gated proton channel currents. *J Physiol* 586:2477–2486.
44. Sasaki M, Takagi M, Okamura Y (2006) A voltage sensor-domain protein is a voltage-gated proton channel. *Science* 312:589–592.
45. López-González I, et al. (2014) Membrane hyperpolarization during human sperm capacitation. *Mol Hum Reprod* 20:619–629.
46. Ren D, et al. (2001) A sperm ion channel required for sperm motility and male fertility. *Nature* 413:603–609.
47. Kirichok Y, Navarro B, Clapham DE (2006) Whole-cell patch-clamp measurements of spermatozoa reveal an alkaline-activated Ca^{2+} channel. *Nature* 439:737–740.
48. Darszon A, Nishigaki T, Beltran C, Trevino CL (2011) Calcium channels in the development, maturation, and function of spermatozoa. *Physiol Rev* 91:1305–1355.
49. Espinosa F, Darszon A (1995) Mouse sperm membrane potential: Changes induced by Ca^{2+}. *FEBS Lett* 372:119–125.
50. Torres-Flores V, Picazo-Juarez G, Hernandez-Rueda Y, Darszon A, Gonzalez-Martinez MT (2011) Sodium influx induced by external calcium chelation decreases human sperm motility. *Hum Reprod* 26:2626–2635.
51. Lewis RJ, Garcia ML (2003) Therapeutic potential of venom peptides. *Nat Rev Drug Discov* 2:790–802.
52. Netirojjanakul C, Miranda LP (2017) Progress and challenges in the optimization of toxin peptides for development as pain therapeutics. *Curr Opin Chem Biol* 38:70–79.
53. Zoppino FC, Halon ND, Bustos MA, Pavarotti MA, Mayorga LS (2012) Recording and sorting live human sperm undergoing acrosome reaction. *Fertil Steril* 97:1309–1315.
54. Seredenina T, Demaurex N, Krause KH (2015) Voltage-gated proton channels as novel drug targets: From NADPH oxidase regulation to sperm biology. *Antioxid Redox Signal* 23:490–513.
55. Murphy R, DeCoursey TE (2006) Charge compensation during the phagocyte respiratory burst. *Biochim Biophys Acta* 1757:996–1011.
56. Campos FV, Chanda B, Beirao PS, Bezanilla F (2008) Alpha-scorpion toxin impairs a conformational change that leads to fast inactivation of muscle sodium channels. *J Gen Physiol* 132:251–263.
57. Wang J, et al. (2011) Mapping the receptor site for alpha-scorpion toxins on a Na^+ channel voltage sensor. *Proc Natl Acad Sci USA* 108:15426–15431.
58. Hong L, Singh V, Wulff H, Tombola F (2015) Interrogation of the intersubunit interface of the open Hv1 proton channel with a probe of allosteric coupling. *Sci Rep* 5:14077.
59. Decoursey TE (2003) Voltage-gated proton channels and other proton transfer pathways. *Physiol Rev* 83:475–579, and erratum (2004) 84:1479.
60. Jungo F, Bougueleret L, Xenarios I, Poux S (2012) The UniProtKB/Swiss-Prot Tox-Prot program: A central hub of integrated venom protein data. *Toxicon* 60:551–557.
61. Musset B, Decoursey T (2012) Biophysical properties of the voltage gated proton channel H_V1. *Wiley Interdiscip Rev Membr Transp Signal* 1:605–620.
62. Musset B, et al. (2012) NOX5 in human spermatozoa: Expression, function, and regulation. *J Biol Chem* 287:9376–9388.